Cavitation in the U9-400 Kaplan turbine model at BEP and PL conditions near cavitation breakdown

Citation for the original published paper (version of record):
Arabnejad Khanouki, M., Nilsson, H., Everyd Bensow, R. (2025). Cavitation in the U9-400 Kaplan turbine model at BEP and PL conditions near cavitation breakdown. 10TH IAHR WORKGROUP MEETING ON CAVITATION AND DYNAMIC PROBLEMS IN HYDRAULIC MACHINERY AND SYSTEMS, 1561. http://dx.doi.org/10.1088/1755-1315/1561/1/012003

(article starts on next page)

IOP Conference Series:
Earth and
Environmental Science

Cavitation in the U9-400 Kaplan turbine model at BEP and PL conditions near cavitation breakdown

To cite this article: Mohammad Hossein Arabnejad *et al* 2025 *IOP Conf. Ser.: Earth Environ. Sci.* **1561** 012003

IOP Conf. Series: Earth and Environmental Science **1561** (2025) 012003 doi:10.1088/1755-1315/1561/1/012003

Cavitation in the U9-400 Kaplan turbine model at BEP and PL conditions near cavitation breakdown

Mohammad Hossein Arabnejad, Håkan Nilsson and Rickard E. Bensow

Department of Mechanics and Maritime Sciences, Chalmers University of Technology, 41296 Gothenburg, Sweden

E-mail: `hakan.nilsson@chalmers.se`

Abstract. This study employs highly resolved CFD to analyze cavitation near cavitation breakdown in a Kaplan turbine model known as U9-400. Both BEP (Best Efficiency Point) and PL (Part-Load) conditions are examined. A comparison is made with data from experiments, provided by Vattenfall, which include high-speed camera recordings of cavitation regions between the blades, and the associated efficiency loss caused by cavitation breakdown. It is shown that the numerical results successfully replicate the experimentally observed cavitation and accurately predict the efficiency reduction. Additionally, we explore the underlying causes of the efficiency reduction near cavitation breakdown, identifying it as a consequence of the diminished pressure difference between the suction and pressure sides of the runner blades.

1. Introduction

Water turbines are to a greater extent used for regulating the electrical grid, resulting in more frequent operation under off-design conditions. To support this flexibility in operation, it is essential to broaden the operating range of the hydraulic turbines. A key challenge is the appearance of cavitation, which arises when a reduction in pressure causes vapor formation. Cavitation can severely degrade the efficiency, generate vibrations, and lead to material damage through cavitation erosion [1]. Consequently, understanding cavitation formation and its impact on turbine performance and reliability is of critical importance.

Numerical simulations have proven to be valuable tools for studying cavitation behavior, as they offer detailed insights into the flow field and allow for the analysis of complex phenomena [2]. In this study, we apply such methods to examine the cavitating flow in the Kaplan turbine model referred to as U9-400. Our objective is to enhance the knowledge of cavitation close to cavitation breakdown during BEP and PL conditions. We begin by comparing the simulation results with experimental data, which confirms that the simulations effectively reproduce the flow features. We then use the simulation data to explore the fundamental reasons behind the performance degradation observed as cavitation breakdown appears.

2. Case and numerical set-up

We study the U9-400 Kaplan turbine model, which is shown in Fig. 1 together with a description of the different parts and the inlet and outlet boundary patches. The runner blade tip and hub clearances are included (the hub clearances only partially at the leading and trailing edges). The flow rate is set at the inlet and the pressure is adjusted at the outlet so that the pressures in the draft tube in the simulation and the experiment are the same. We employ an LES approach together with a homogeneous mixture model including cavitation mass transfer. The value of the vapour pressure is set up according to the water temperature in the experiment. The hexahedral mesh is generated with Pointwise v18.3. The number of cells and average y^+ values in the different regions are 16.3M and $y^+ \sim 21$ for SC+SV+GV, 6.6M and $y^+ \sim 20$ for RU, 5.8M and $y^+ \sim 27$ for DT, summing up to 28.6M and and $y^+ \sim 22$ in total.

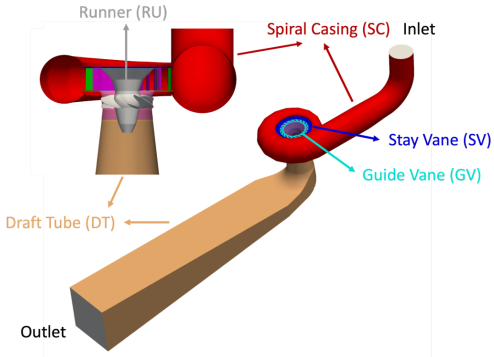

Figure 1: The U9-400 Kaplan turbine model, its parts, and inlet and outlet boundary patches.

A modified interPhaseChangeFoam solver [3, 4] from OpenFOAM-2.2.x [5] has been adopted. It solves the incompressible Navier-Stokes equations for iso-thermal two-phase flows. Considering the phases to be a homogeneous mixture and using Large Eddy Simulations, the governing equations read

$$\frac{\partial}{\partial t}(\bar{\rho}) + \nabla \cdot (\bar{\rho}\tilde{\mathbf{u}}) = 0, \tag{1}$$

$$\frac{\partial}{\partial t}(\bar{\rho}\tilde{\mathbf{u}}) + \nabla \cdot (\bar{\rho}\tilde{\mathbf{u}} \otimes \tilde{\mathbf{u}}) + \nabla \cdot ([\bar{p}\mathbf{I} - \bar{\tau}]) + \nabla \cdot (\tau_{sgs}) = 0, \tag{2}$$

where $\bar{\rho}$ is the phasic filtered density, $\tilde{\mathbf{u}}$ is the Favre phasic filtered velocity vector, and $\bar{p}$ is the phasic filtered pressure. Further, $\mathbf{I}$, $\bar{\tau}$ and τ_{sgs} are, respectively, the identity tensor, the viscous stress tensor and the sub-grid scale tensor in the mixture momentum equations. Assuming a homogeneous mixture and a constant dynamic viscosity for each phase (μ^k), the viscous stress tensor of the mixture can be obtained as

$$\bar{\tau} = (\sum_{k=1}^{2} \alpha^k \mu^k)\bar{S}, \tag{3}$$

incorporating the mixture strain tensor $\bar{S}$. The effects of the sub-grid scale turbulence is accounted for using the WALE (wall-adapting local eddy-viscosity) model proposed by Nicoud and Ducros [6]. The sub-grid scale tensor is thus given by

$$\tau_{sgs} - \frac{2}{3}k_{sgs}\mathbf{I} = -2\nu_{sgs}\bar{S}. \tag{4}$$

Here, the sub-grid scale turbulent viscosity, ν_{sgs}, is given by the sub-grid kinetic energy, k_{sgs}, as

$$\nu_{sgs} = C_k \Delta \sqrt{k_{sgs}}, \tag{5}$$

where Δ is the cell length scale, $C_k = 1.6$ is a model constant, and k_{sgs} can be calculated from

$$k_{sgs} = \left(\frac{C_w^2 \Delta}{C_k}\right)^2 \frac{(\tilde{S}^d \tilde{S}^d)^3}{\left(\left(\tilde{S}\tilde{S}\right)^{5/2} + \left(\tilde{S}^d \tilde{S}^d\right)^{5/4}\right)^2}. \tag{6}$$

Here $\tilde{S}$ is the resolved-scale strain rate tensor and $\tilde{S}^d$ is the traceless symmetric part of the square of the velocity gradient tensor. An additional model constant is introduced as $C_w = 0.325$.

Transport Equation Modelling (TEM) is adopted to capture the cavitation dynamics, for which the liquid volume fraction (α^l) transport equation reads

$$\frac{\partial}{\partial t}(\alpha^l \bar{\rho}^l) + \nabla \cdot (\alpha^l \bar{\rho}^l \tilde{\mathbf{u}}) = \dot{m}. \tag{7}$$

Here, the mass transfer term, $\dot{m}$, involves vaporization and condensation, for which the Schnerr-Sauer model [7] is adopted. Condensation, $\dot{m}_{\alpha_c^l}$, and vaporization, $\dot{m}_{\alpha_v^l}$, gives the mass transfer as

$$\dot{m} = \alpha^l \left(\dot{m}_{\alpha_v^l} - \dot{m}_{\alpha_c^l}\right) + \dot{m}_{\alpha_c^l}. \tag{8}$$

The condensation and vaporization terms are given by

$$\dot{m}_{\alpha_c^l} = C_c \alpha^l \frac{3\bar{\rho}^l \bar{\rho}^v}{\bar{\rho} R_B} \times \sqrt{\frac{2}{3\bar{\rho}^l}} \sqrt{\frac{1}{|\bar{p} - p_v|}} max\left(\bar{p} - p_v, 0\right), \tag{9}$$

$$\dot{m}_{\alpha_v^l} = C_v \left(1 + \alpha_{Nuc} - \alpha^l\right) \frac{3\bar{\rho}^l \bar{\rho}^v}{\bar{\rho} R_B} \times \sqrt{\frac{2}{3\bar{\rho}^l}} \sqrt{\frac{1}{|\bar{p} - p_v|}} min\left(\bar{p} - p_v, 0\right). \tag{10}$$

Here, $C_c = C_v = 1$, p_v is the vapor pressure (set up according to the water temperature in the experiment), α_{Nuc} is the initial volume fraction of the nuclei, and R_B is the radius of the nuclei, given by

$$R_B = \sqrt[3]{\frac{3}{4\pi n_0} \frac{(1 + \alpha_{Nuc} - \alpha^l)}{\alpha^l}}. \tag{11}$$

The initial volume fraction of the nuclei is given by

$$\alpha_{Nuc} = \frac{\frac{\pi n_0 d_{Nuc}^3}{6}}{1 + \frac{\pi n_0 d_{Nuc}^3}{6}}, \tag{12}$$

assuming an average number of nuclei per cubic meter of liquid volume of $n_0 = 10^{12}$, and an initial nuclei diameter of $d_{Nuc} = 10^{-5}$.

For the momentum equations, the second-order upwind scheme by Warming and Beam [8] is used for the discretization of the convective terms. For the liquid fraction equation, the convective term is discretized using a first-order upwind scheme. The second-order linear scheme is used for the discretization of the diffusion terms and a second-order implicit scheme is used for the time discretization. A time step of the order of 10^{-4} is used and the simulations are conducted sufficiently long to get stable statistics. The pressure-based PIMPLE approach is adopted to solve the system of equations. Asnaghi [4] and Bensow and Bark [3] give more detailed descriptions of the solution procedure.

Table 1: Efficiency at different cavitation numbers in numerical simulations and experiment.

	PL		BEP	
	$\sigma = 0.31$	$\sigma = 0.2064$	$\sigma = 0.31$	$\sigma = 0.2278$
Num.	84.25%	81.28%	89.18%	79.35%
Exp.	84.13%	83.75%	89.96%	87.04%

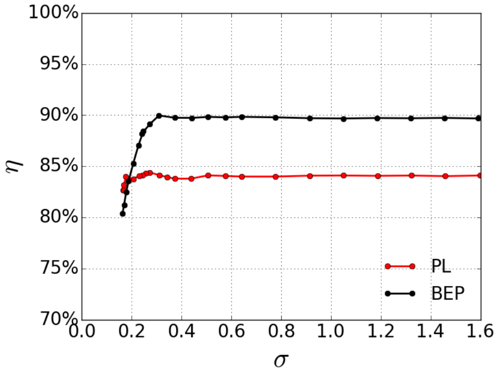

Figure 2: Efficiency at PL and BEP conditions for different cavitation numbers.

2.1. Studied conditions

The simulations are conducted under PL (part load) and BEP (best efficiency point) conditions. The guide vane angle is the same for both conditions, while the runner angle is set at 20 degrees for PL and 26.5 degrees for BEP. Figure 2 illustrates the time-averaged turbine efficiency at PL and BEP conditions for various cavitation numbers in the experiment. It can be observed that the efficiency abruptly decreases for both conditions when the cavitation number falls below 0.3, indicating the onset of cavitation breakdown. Since this study focuses on investigating the cavitation behavior near the onset of cavitation breakdown, two cavitation numbers are simulated for each PL and BEP condition. The first simulation is performed at $\sigma = 0.31$, which is prior to the onset of cavitation, while the second simulation is conducted for the cavitation number lower than 0.30 ($\sigma = 0.2064$ for PL and $\sigma = 0.2278$ for BEP) in which a drop in the efficiency can be seen. The cavitation number is calculated as done by Arabnejad et al. [2], at the draft tube outlet.

3. Results

Table 1 presents the efficiency for the two investigated cavitation numbers under the PL and BEP conditions in both simulations and experiment. It is clear that the simulations accurately capture the efficiency decrease observed in the experiment as a result of a reduced cavitation number. However, the simulations show a more substantial efficiency drop compared to the experiment. Furthermore, both experimental and numerical results indicate a more pronounced performance drop for the BEP condition compared to the PL condition. The reasons behind this behavior will be explained later.

Fig. 3 shows the cavitating regions observed in both the experiments and simulations for the studied cases. At high cavitation numbers and under PL conditions (Fig. 3a), the experimental image reveals two cavitation regions around the runner: the hub vortex (HVC) and the tip vortex (TVC). The simulation results can successfully capture these cavitating regions. Additionally, a significant amount of cavitation can be seen in the rotating vortex rope (RVRC) in the numerical results (the experimental recording did not cover the vortex rope). When the cavitation number

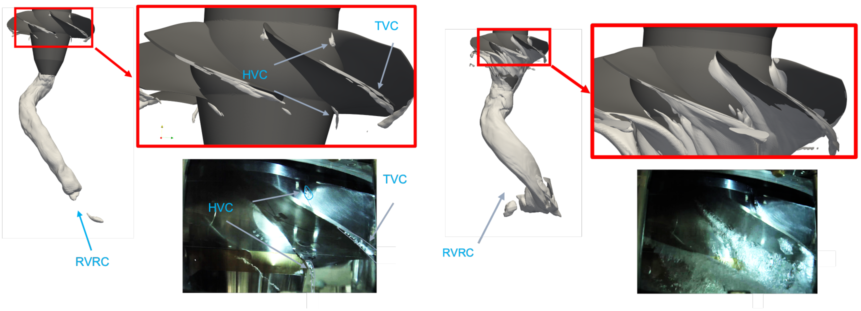

(a) PL, $\sigma = 0.31$ (b) PL, $\sigma = 0.02064$

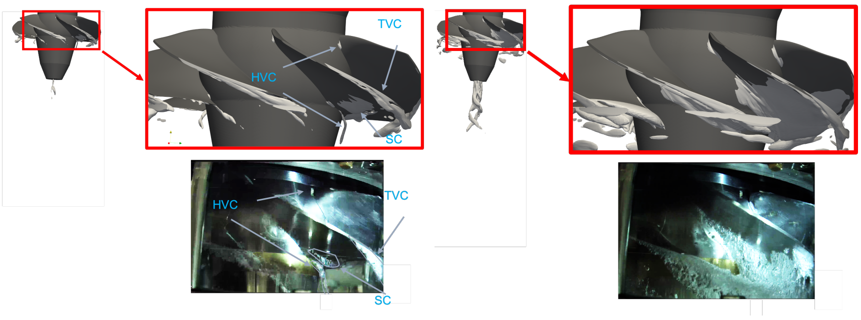

(c) BEP, $\sigma = 0.31$ (d) BEP, $\sigma = 0.2278$

Figure 3: Cavitating regions in the numerical simulations and experimental observations.

is reduced (Fig. 3b), the cavitation regions in the hub and tip grow, eventually merging and connecting with the cavitation regions in the RVRC. The experimental image for the BEP condition and high cavitation number (Fig. 3c) demonstrates that cavitation, similar to the PL condition and high cavitation number (Fig. 3a), can be observed in the hub and tip vortices (HVC and TVC in Fig. 3c). Furthermore, cavitation is visible on the blade near the trailing edge (region SC in Fig. 3c). The numerical results for this condition show that these cavitation regions can be accurately predicted. The results also indicate that as the cavitation number decreases (Fig. 3d), the cavitation near the trailing edge expands, covering a substantial portion of the blade, and some cavitation can be observed in the downstream vortex formed by the runner.

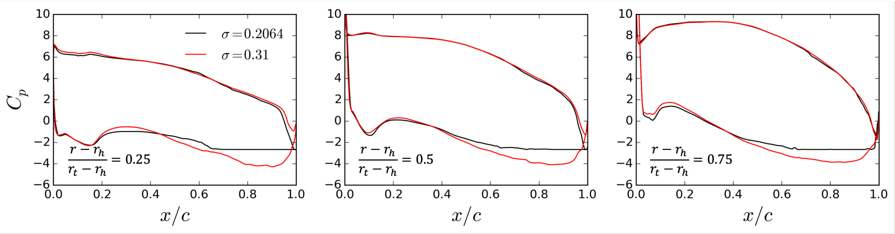

(a) PL

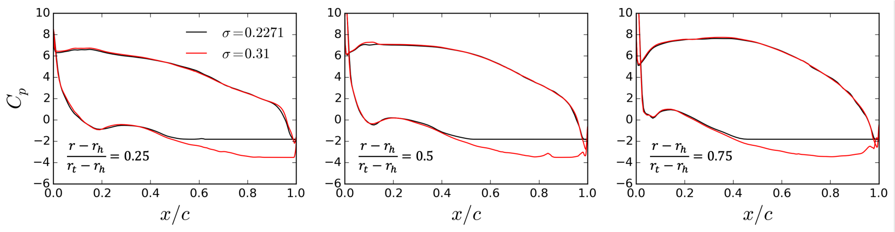

(b) BEP

Figure 4: Pressure coefficient around the runner blade at three radial sections for PL and BEP conditions and different cavitation numbers.

To investigate the cause of the performance drop attributed to cavitation, as presented in Table 1, Figure 4 illustrates the pressure coefficient, denoted as C_p, at three radial sections under low and high cavitation numbers at PL and BEP conditions. These radial sections are positioned at $\frac{r-r_h}{r_t-r_h} = 0.25, 0.5, 0.75$, where r, r_h, and r_t represent the radius at the section, the radius at the hub of the runner blade, and the radius at the tip of the blade, respectively. In the figures, the top lines indicate higher C_p values, corresponding to the pressure side, while the bottom lines represent the suction side. At the PL condition (Fig. 4a), a comparison of the plots for $\sigma = 0.31$ and $\sigma = 0.2064$ reveals that the presence of additional cavitation does not significantly affect C_p on the pressure side. However, increased cavitation results in a flattened distribution of C_p near the trailing edge of the suction side. This distribution arises due to a uniform pressure caused by cavitation, which is equal to the vapor pressure near the trailing edge. A similar trend can be observed under BEP conditions. The flattening of the C_p distribution over the suction side reduces the pressure difference between the pressure and suction sides which in turn leads to a reduction in the torque applied to the blade. This can explain the drop in the turbine efficiency (shown in Table 1) as the cavitation number decreases. Additionally, the results indicate that the flattening of C_p due to cavitation is more pronounced under BEP conditions compared to PL conditions. This can be attributed to a larger area of the suction side being affected by decreasing the cavitation number, resulting in a more significant efficiency drop for the BEP condition which also shown in Table 1.

4. Conclusions

This paper presents numerical simulations of cavitation in the U9-400 Kaplan turbine model at BEP and PL conditions near cavitation breakdown. The objective is to investigate cavitating flows at BEP and PL conditions, with a particular focus on the cavitation conditions near cavitation breakdown. To validate the simulations, we compare the obtained results with the experimental data provided by Vattenfall. This comparison demonstrates that the simulations can successfully reproduce the cavitation patterns observed in the experiments, and accurately predict the efficiency reduction near the cavitation breakdown. Furthermore, the numerical simulation is utilized to explain the efficiency drop caused by cavitation breakdown. Our results indicate that a decrease in the cavitation number near cavitation breakdown leads to a reduction in the pressure difference between the runner blade pressure side (PS) and suction side (SS). This decrease results in a reduction in torque applied to the blades, thereby causing the drop in efficiency near cavitation breakdown. Additionally, the results reveal that the sensitivity of the pressure difference between SS and PS to the cavitation number is greater at BEP conditions compared to PL. This explains the higher sensitivity of efficiency to the cavitation number in the BEP near cavitation breakdown, as observed in both simulations and experiments.

Acknowledgments

The work was financed by Chalmers Energy Area of Advance and the “Swedish Hydropower Centre - SVC”. SVC is established by the Swedish Energy Agency, Energiforsk and Svenska Kraftnät together with Luleå University of Technology, The Royal Institute of Technology, Chalmers University of Technology and Uppsala University, www.svc.nu.

We would like to thank Carl-Maikel Högström and Berhanu Mulu from Vattenfall Research and Development AB for providing the experimental data used in this study.

The computations were enabled by resources provided by the Swedish National Infrastructure for Computing (SNIC) at NSC and C3SE partially funded by the Swedish Research Council through grant agreement no. 2018-05973.

References

[1] F. Avellan. Introduction to cavitation in hydraulic machinery. Technical report, Politehnica University of Timișoara, 2004.

[2] M.H. Arabnejad, H. Nilsson, and R. E. Bensow. Investigation of flow-induced instabilities in a francis turbine operating in non-cavitating and cavitating part-load conditions. *Fluids*, 8(2):61, 2023.

[3] R.E. Bensow and G. Bark. Implicit LES predictions of the cavitating flow on a propeller. *Journal of Fluids Engineering*, 132(4):041302, 2010.

[4] A. Asnaghi. *Developing computational methods for detailed assessment of cavitation on marine propellers.* Licentiate thesis, 2015.

[5] H. Weller, G. Tabor, H. Jasak, and C. Fureby. A tensorial approach to computational continuum mechanics using object-oriented techniques. *Computers in physics*, 12(6):620–631, 1998.

[6] F. Nicoud and F. Ducros. Subgrid-scale stress modelling based on the square of the velocity gradient tensor. *Flow, turbulence and Combustion*, 62(3):183–200, 1999.

[7] J. Sauer. Instationär kavitierende strömungen-ein neues modell, basierend auf front capturing (vof) und blasendynamik. *Diss., Uni Karlsruhe*, 2000.

[8] RF Warming and Richard M Beam. Upwind second-order difference schemes and applications in aerodynamic flows. *AIAA Journal*, 14(9):1241–1249, 1976.